nature materials

Article

https://doi.org/10.1038/s41563-022-01386-z

Crossover from Ising- to Rashba-type superconductivity in epitaxial Bi_2Se_3/monolayer $NbSe_2$ heterostructures

Received: 11 January 2022

Accepted: 21 September 2022

Published online: 27 October 2022

Check for updates

Hemian Yi[1,7], Lun-Hui Hu[1,7], Yuanxi Wang[1,2,7], Run Xiao[1], Jiaqi Cai[3], Danielle Reifsnyder Hickey[4,5], Chengye Dong[5], Yi-Fan Zhao[1], Ling-Jie Zhou[1], Ruoxi Zhang[1], Anthony R. Richardella[1], Nasim Alem[5], Joshua A. Robinson[5], Moses H. W. Chan[1], Xiaodong Xu[3,6], Nitin Samarth[1], Chao-Xing Liu[1] and Cui-Zu Chang[1]

A topological insulator (TI) interfaced with an *s*-wave superconductor has been predicted to host topological superconductivity. Although the growth of epitaxial TI films on *s*-wave superconductors has been achieved by molecular-beam epitaxy, it remains an outstanding challenge for synthesizing atomically thin TI/superconductor heterostructures, which are critical for engineering the topological superconducting phase. Here we used molecular-beam epitaxy to grow Bi_2Se_3 films with a controlled thickness on monolayer $NbSe_2$ and performed in situ angle-resolved photoemission spectroscopy and ex situ magnetotransport measurements on these heterostructures. We found that the emergence of Rashba-type bulk quantum-well bands and spin-non-degenerate surface states coincides with a marked suppression of the in-plane upper critical magnetic field of the superconductivity in Bi_2Se_3/monolayer $NbSe_2$ heterostructures. This is a signature of a crossover from Ising- to Rashba-type superconducting pairings, induced by altering the Bi_2Se_3 film thickness. Our work opens a route for exploring a robust topological superconducting phase in TI/Ising superconductor heterostructures.

Since the discovery of heavy-fermion superconductors and high-temperature superconductors in cuprate–perovskite ceramics, research on unconventional (that is, non-*s*-wave) superconductivity continues to reveal new questions and challenges. An exciting possibility is topological superconductivity (TSC) in hybrid structures where a topological insulator (TI) is proximally coupled to a conventional *s*-wave superconductor[1]. A primary barrier to the growth of TI films on *s*-wave superconductors (or vice versa) lies in the difficulty of achieving an atomically sharp interface due to a host of experimental challenges such as chemical reactivity and uncontrolled nucleation. To date, the most successful realization of TIs interfaced with *s*-wave superconductors is the molecular-beam epitaxy (MBE)-grown Bi_2Se_3 or Bi_2Te_3 films on bulk crystals of superconducting $NbSe_2$ (refs. [2–7]). However, for device fabrication and potential application in topological quantum computations, MBE-grown $NbSe_2$ films are preferred over $NbSe_2$ bulk crystals.

[1]Department of Physics, The Pennsylvania State University, University Park, PA, USA. [2]Department of Physics, University of North Texas, Denton, TX, USA. [3]Department of Physics, University of Washington, Seattle, WA, USA. [4]Department of Chemistry, The Pennsylvania State University, University Park, PA, USA. [5]Department of Materials Science and Engineering, The Pennsylvania State University, University Park, PA, USA. [6]Department of Materials Science and Engineering, University of Washington, Seattle, WA, USA. [7]These authors contributed equally: Hemian Yi, Lun-Hui Hu, Yuanxi Wang. e-mail: cxc955@psu.edu

https://doi.org/10.1038/s41563-022-01386-z

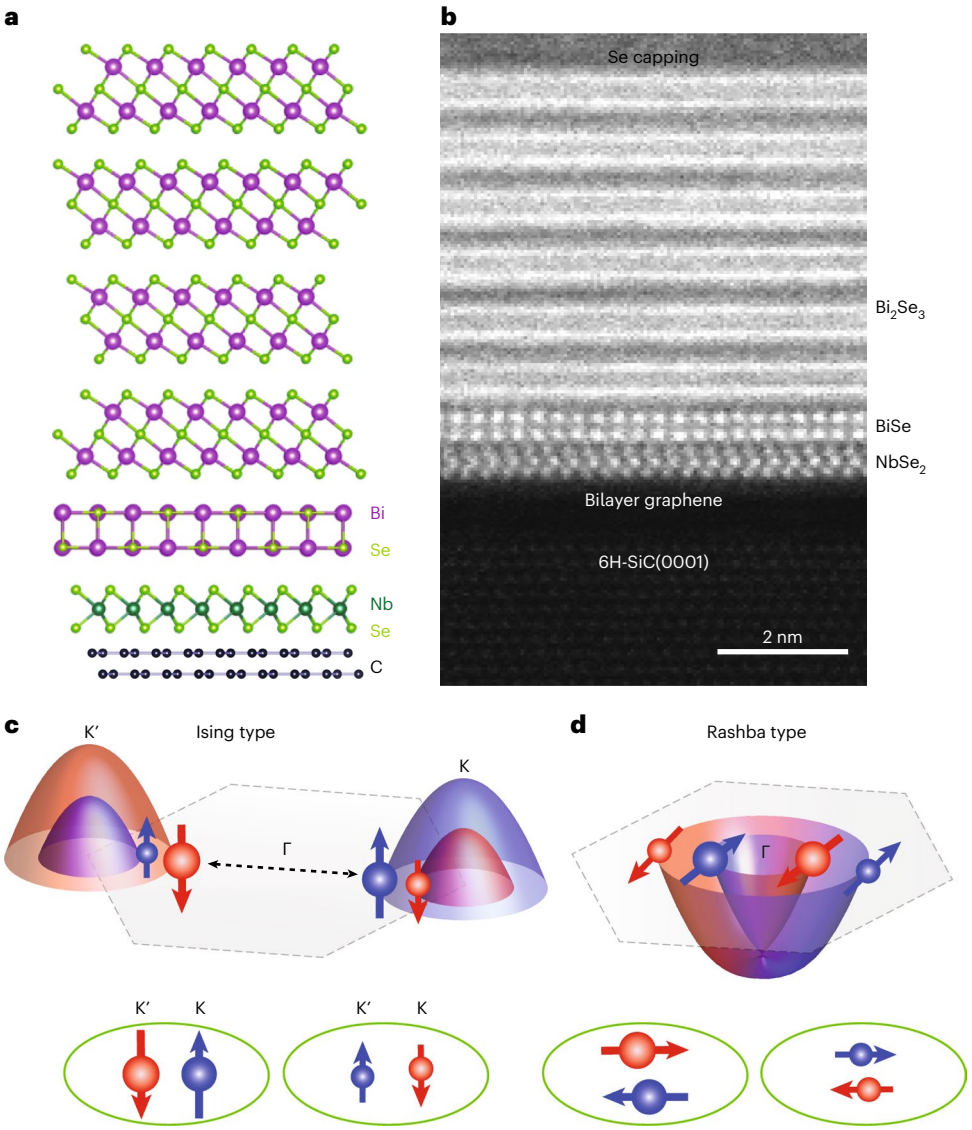

Fig. 1 | MBE-grown Bi_2Se_3/monolayer $NbSe_2$ heterostructures on epitaxial bilayer graphene. a, Schematic of the 4QL Bi_2Se_3/monolayer $NbSe_2$ heterostructure on bilayer graphene. **b**, Cross-sectional ADF-STEM image of the 6QL Bi_2Se_3/monolayer $NbSe_2$ heterostructure on bilayer graphene. The atomic structures of monolayer $NbSe_2$ and Bi_2Se_3 layers cannot be simultaneously resolved, suggesting a misorientation between these two layers. **c**,**d**, Schematic of the Ising-type (**c**) and Rashba-type (**d**) pairing symmetry in superconductors. For the Ising-type superconductor (for example, monolayer $NbSe_2$), the electrons are near the K and K′ valleys with spins pinned to the out-of-plane direction. However, for the Rashba-type superconductor (for example, Bi_2Se_3/monolayer $NbSe_2$), the electrons are near the Γ point with spins pinned to the in-plane direction.

Prior studies have demonstrated that superconductivity in atomically thin films, particularly monolayer $NbSe_2$ films, persists under in-plane magnetic fields far beyond the Pauli limit (H_P) due to its Ising-type superconducting pairing symmetry[8,9]. In Ising-type superconductors, electron spins are pinned to the out-of-plane direction due to the breaking of the SU(2) spin rotation via the strong Ising-type spin–orbit interaction. This property makes the breaking of Cooper pairs difficult under an in-plane magnetic field. The TSC phase has also been theoretically predicted in Ising-type superconductors, particularly in transition metal dichalcogenides[10–12]. We may anticipate that a robust TSC phase appears in a TI/Ising superconductor (for example, Bi_2Se_3/monolayer $NbSe_2$) heterostructure due to its complex spin–orbit-coupling form. However, experimental studies along this direction are lacking to date, primarily because the Ising-type superconductor becomes non-superconducting after being covered by a TI film.

In this work, we used MBE to fabricate Bi_2Se_3/monolayer $NbSe_2$ heterostructures with different Bi_2Se_3 thicknesses and performed in situ angle-resolved photoemission spectroscopy (ARPES) and ex situ electrical transport on these heterostructures. We observed that the Dirac surface states (SSs) emerge when the thickness of Bi_2Se_3 is greater than three quintuple layers (QLs), which is lower compared with previous studies of thicker (that is, ≥6QL) Bi_2Se_3 films grown on sapphire[13], bilayer graphene[14] and Si(111) (ref. [15]) substrates. We found that Rashba-type conduction bands and spin-non-degenerate Dirac SSs appear when the Bi_2Se_3 thickness is greater than 2QL. These features observed in ARPES studies were found to agree well with our first-principles calculations. Moreover, we found that the in-plane upper critical magnetic field (that is, $H_{c2,\parallel}/H_P$) of the superconducting Bi_2Se_3/monolayer $NbSe_2$ heterostructures is greatly reduced when the Rashba-type bulk conduction bands and Dirac SSs emerge, implying the crossover from Ising- to Rashba-type superconductivity.

https://doi.org/10.1038/s41563-022-01386-z

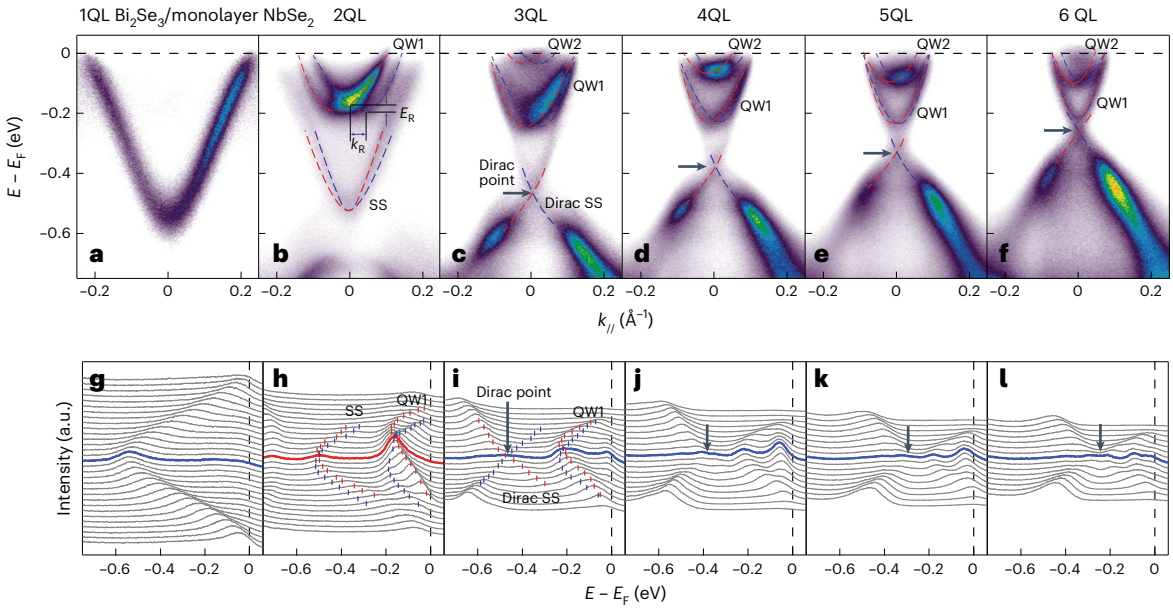

Fig. 2 | ARPES band maps of Bi_2Se_3/monolayer $NbSe_2$ heterostructures. **a**–**f**, ARPES results of *m*QL Bi_2Se_3/monolayer $NbSe_2$ heterostructures with $m = 1$ (**a**), $m = 2$ (**b**), $m = 3$ (**c**), $m = 4$ (**d**), $m = 5$ (**e**) and $m = 6$ (**f**). **g**–**l**, Corresponding energy distribution curves of the ARPES results in **a**–**f**, respectively. The Rashba-type SSs and Rashba-type bulk QW states (that is, QW1 and QW2) are highlighted by the red and blue dashed lines, respectively. The ARPES experiments were performed at room temperature. For the Bi_2Se_3 thickness greater than 3QL, the Dirac point is formed, and the second-lowest Rashba-type bulk QW states (that is, QW2) appear.

The establishment of the MBE growth of Bi_2Se_3/monolayer $NbSe_2$ heterostructures and the demonstration of crossover from two-dimensional (2D) Ising- to three-dimensional (3D) bulk Rashba-type superconductivity in these heterostructures will facilitate the investigations of the robust TSC phase in TI/Ising-type superconductor heterostructures.

The 2H phase of $NbSe_2$ bulk crystal is a well-studied *s*-wave superconductor[16]. Its unit cell consists of the Se–Nb–Se trilayer structure. Monolayer $NbSe_2$ has an out-of-plane mirror symmetry but breaks the in-plane inversion symmetry, which leads to Ising-type superconductivity in monolayer $NbSe_2$ (refs. [8,9]). Bi_2Se_3 is a prototypical 3D TI, where a single Dirac cone exists at the Γ point of the first Brillouin zone[17,18]. The unit cell of Bi_2Se_3 consists of the Se–Bi–Se–Bi–Se QL structure. Since both $NbSe_2$ and Bi_2Se_3 are Se-based layered materials and share the same hexagonal lattice structure, it is natural to use MBE to synthesize both $NbSe_2$ and Bi_2Se_3 layers to form Bi_2Se_3/$NbSe_2$ heterostructures (Fig. 1a and Extended Data Fig. 1). However, as noted above, the superconductivity of MBE-grown $NbSe_2$ films usually fades away after the coverage of Bi_2Se_3 films. By carefully optimizing the growth protocols (Methods), we successfully retained the superconductivity in Bi_2Se_3/monolayer $NbSe_2$ heterostructures. We first characterized Bi_2Se_3/monolayer $NbSe_2$ heterostructures using annular dark-field scanning transmission electron microscopy (ADF-STEM) (Fig. 1b and Extended Data Fig. 2). In addition to the prominent Bi_2Se_3 QL and $NbSe_2$ trilayer structures, we observed a BiSe bilayer with a cubic lattice structure at the Bi_2Se_3/$NbSe_2$ interface. This observation is consistent with prior studies on Bi_2Se_3/bulk $NbSe_2$ (ref. [19]). The formation of this cubic BiSe layer is presumably stabilized by the large work function of the monolayer $NbSe_2$ underneath.

As noted above, monolayer $NbSe_2$ is an Ising-type superconductor[8,9], in which the broken in-plane inversion symmetry can generate an out-of-plane spin polarization under an effective Zeeman field (that is, Ising-type spin–orbit interaction), which induces a Zeeman-type spin splitting at the bulk valence band maxima located at the K and K′ points with opposite signs (Fig. 1c). Therefore, the intervalley Cooper pairs in monolayer $NbSe_2$ involve two electrons with locked opposite out-of-plane spins, which are referred to as Ising-type pairing. Superconductivity can also arise in materials with a Rashba-type band structure, where the spins of the electrons are pinned to the in-plane direction (Fig. 1d). Cooper pairing between two such electrons with opposite in-plane spins is known as Rashba-type pairing. In our experiment, by depositing Bi_2Se_3 films on top of monolayer $NbSe_2$, Rashba-type conduction bands and Dirac SSs emerge and become superconducting due to the proximity effect. Therefore, Bi_2Se_3/monolayer $NbSe_2$ heterostructures provide a platform to study the crossover between Ising- and Rashba-type pairings in a single system.

We next performed in situ ARPES measurements on *m*QL Bi_2Se_3/monolayer $NbSe_2$ heterostructures by systematically increasing *m*. For monolayer $NbSe_2$ (that is, $m = 0$), a hole pocket that crosses the Fermi energy near the Γ point was observed (Extended Data Fig. 3), consistent with prior studies[20,21]. After the deposition of 1QL Bi_2Se_3 (that is, $m = 1$) on monolayer $NbSe_2$, the ARPES band map shows a near-parabolic band dispersion, which is analogous to that of 1QL Bi_2Se_3 directly grown on epitaxial bilayer graphene substrates[14]. Compared with 1QL Bi_2Se_3 grown on graphene, 1QL Bi_2Se_3/monolayer $NbSe_2$ is more electron doped. The bulk conduction band minimum is at $(E - E_F) \approx -0.55$ eV (Fig. 2a,g). A gap of ~0.73 eV was observed for the $m = 1$ sample (Extended Data Fig. 3). With increasing *m*, the hybridization gap between the top and bottom SSs decreases. The gap is ~0.18 eV for the $m = 2$ sample. Furthermore, we observed Rashba-type SSs for the $m = 2$ sample (Fig. 2b,h), implying symmetry-inequivalent top and bottom SSs (ref. [14]). For the $m \geq 3$ samples, the SSs become gapless, a signature of crossover from 2D to 3D TI regimes[22] (Fig. 2c,i). The crossover thickness in Bi_2Se_3/$NbSe_2$ heterostructures is found to be 3QL. This is greatly lower than 6QL observed for Bi_2Se_3 films grown on other substrates including $NbSe_2$ bulk crystals[2,3,13–15]. With increasing *m*, the chemical potential gradually approaches the Dirac point (Fig. 2d–f,j–l).

In addition to the reduced 2D to 3D crossover thickness, the bulk conduction bands of Bi_2Se_3 films grown on monolayer $NbSe_2$ form quantum-well (QW) states for $m \geq 2$ (Fig. 2b–f,h–l). Distinct from the QW states observed in Bi_2Se_3 films on sapphire[13], bilayer graphene[14], Si(111)[15] and $NbSe_2$ bulk crystals[2,3], the QW states in *m*QL Bi_2Se_3/monolayer $NbSe_2$ heterostructures exhibit a Rashba-type band splitting,

https://doi.org/10.1038/s41563-022-01386-z

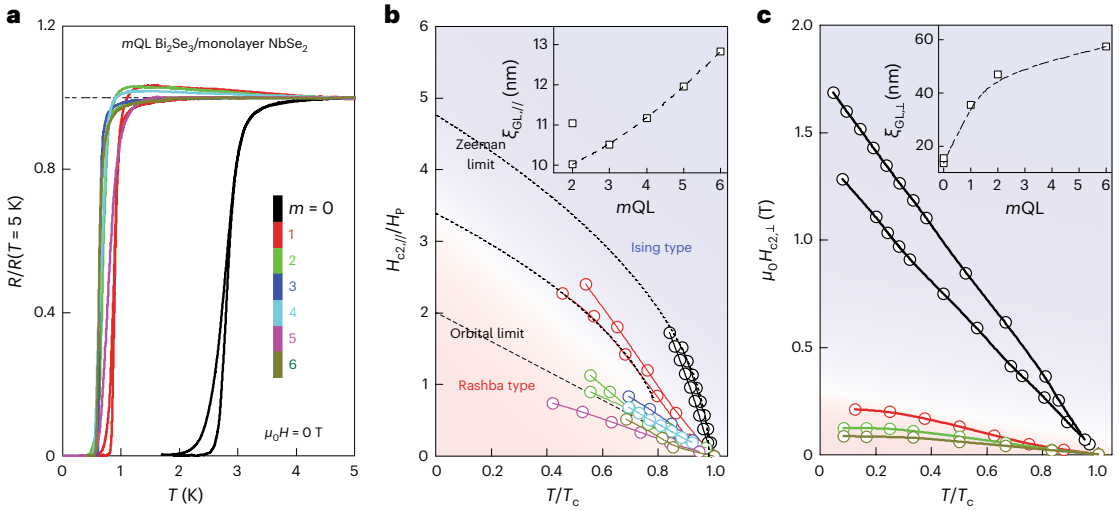

Fig. 3 | Crossover from Ising- to Rashba-type pairing symmetry in Bi_2Se_3/monolayer $NbSe_2$ heterostructures. a, R–T curves of the mQL Bi_2Se_3/monolayer $NbSe_2$ heterostructures under zero magnetic field. R is normalized to the normal-state resistance at $T = 5$ K. The superconducting transition temperature T_c is suppressed for $m \geq 1$. The enlarged R–T curves are shown in Supplementary Fig. 1. **b**, In-plane upper critical magnetic field normalized to the Pauli paramagnetic limit, $H_{c2,\parallel}/H_P$, as a function of reduced temperature T/T_c for mQL Bi_2Se_3/monolayer $NbSe_2$ heterostructures. **c**, Out-of-plane upper critical magnetic field $H_{c2,\perp}$ as a function of reduced temperature T/T_c for mQL Bi_2Se_3/monolayer $NbSe_2$ heterostructures. The insets in **b** and **c** are the in-plane and out-of-plane GL coherence lengths $\xi_{GL,\parallel}$ and $\xi_{GL,\perp}$ as a function of m, respectively. The shadings in **b** and **c** indicate the crossover from Ising-type superconductivity (light blue) to Rashba-type superconductivity (light red). Two $m = 0$ samples are included in **a**–**c**. Two $m = 1$ and $m = 2$ samples are included in **a** and **b**.

similar to a recent theoretical prediction based on Bi_2Se_3/monolayer $PtSe_2$ heterostructures[23]. To estimate the Rashba coupling strength α_R of the lowest QW states (Fig. 2, QW1), we defined the energy difference between the minimum of QW1 states and Rashba band crossing at the Γ point as E_R and the momentum offset of two Rashba bands as k_R (Fig. 2b). Consequently, the Rashba splitting parameter for a local parabolic dispersion is approximated by $\alpha_R = 2E_R/k_R$. For the $m = 2$ sample, $E_R \approx 0.019$ eV and $k_R \approx 0.038$ Å^{-1}, yielding $\alpha_R \approx 1.0$ eV Å. The value of α_R in the 2QL Bi_2Se_3/monolayer $NbSe_2$ heterostructure is comparable to that of the Rashba splitting of Bi_2Se_3 bulk conduction QW states[24–27]. With increasing m, α_R monotonically decreases and almost vanishes in the $m = 6$ sample, but the Rashba splitting of the second-lowest bulk QW states (Fig. 2, QW2) remains large in the $3 \leq m \leq 6$ samples (Fig. 2 and Extended Data Fig. 4). The appearance of Rashba-type bulk QW bands and/or spin-non-degenerate Dirac SSs can together influence the occurrence of the superconducting proximity effect between Bi_2Se_3 and monolayer $NbSe_2$ films, as discussed below.

Next, we focused on the transport measurements of mQL Bi_2Se_3/monolayer $NbSe_2$ heterostructures. As shown in Fig. 2, the chemical potential crosses the Rashba-type bulk bands and/or spin-non-degenerate Dirac SSs, and the electrons possess in-plane spin polarization in both cases (Fig. 1d). When the superconducting proximity effect occurs between monolayer $NbSe_2$ film and mQL Bi_2Se_3 films, the Ising-type pairing in monolayer $NbSe_2$ film is suppressed and the Rashba-type pairing becomes progressively dominant with increasing m in mQL Bi_2Se_3/monolayer $NbSe_2$ heterostructures. Figure 3a shows the temperature dependence of the normalized longitudinal resistance R of the mQL Bi_2Se_3/$NbSe_2$ heterostructures with $0 \leq m \leq 6$. All these samples show superconductivity, with the superconducting transition temperatures (T_c) decreasing with increasing m. Here we defined T_c as the temperature at which R drops to 50% of the normal-state resistance found at $T = 5$ K. Also, T_c is found to decrease from ~2.8 K for monolayer $NbSe_2$ to ~0.6 K for the $m = 6$ sample[28] (Supplementary Fig. 1). Note that our ARPES band map of the $m = 1$ heterostructure shows a superposition of the electronic band structures of both 1QL Bi_2Se_3 and monolayer $NbSe_2$ (Extended Data Fig. 3). Since the valence band alignment of monolayer $NbSe_2$ does not change in the $m = 0$ and $m = 1$ samples, we can ignore the charge transfer effect between Bi_2Se_3 and monolayer $NbSe_2$ layers. Therefore, the observed superconductivity suppression (that is, T_c reduction) in our Bi_2Se_3/monolayer $NbSe_2$ heterostructures can be primarily attributed to the standard superconducting proximity effect[29] (Supplementary Fig. 2) rather than electron injection across the interface between the Bi_2Se_3 and monolayer $NbSe_2$ layers[30].

We performed the magnetoresistance measurements on these Bi_2Se_3/monolayer $NbSe_2$ heterostructures under in-plane and out-of-plane magnetic fields (Fig. 3b,c). The upper critical magnetic fields $H_{c2,\parallel}$ and $H_{c2,\perp}$ are defined as the magnetic field at which R is ~50% of the normal-state resistance (Extended Data Figs. 5–7). Figure 3b shows the reduced temperature (T/T_c) dependence of the normalized in-plane upper critical magnetic field ($H_{c2,\parallel}/H_P$) for the mQL Bi_2Se_3/monolayer $NbSe_2$ heterostructures with $0 \leq m \leq 6$. For the $m = 0$ sample, the $(H_{c2,\parallel}/H_P)$–(T/T_c) curve near T_c can be fitted by using $H_{c2,\parallel}/H_P \propto \sqrt{1 - T/T_c}$ for a 2D superconductor. When 1QL Bi_2Se_3 is deposited on top of monolayer $NbSe_2$, that is, the $m = 1$ sample, the $(H_{c2,\parallel}/H_P)$–(T/T_c) curve slightly deviates from this square-root-T behaviour, indicating a crossover from 2D to 3D superconductivity[31]. For the $m \geq 2$ samples, the $(H_{c2,\parallel}/H_P)$–(T/T_c) curves can be fitted with $(H_{c2,\parallel}/H_P) \propto (1 - T/T_c)$ for a 3D superconductor. The linear temperature dependence of $H_{c2,\parallel}$ indicates that the orbital effect is dominant rather than the paramagnetic effect for the in-plane pair-breaking magnetic field in the Bi_2Se_3/$NbSe_2$ heterostructures with $m \geq 2$. Given the presence of Rashba-type conduction bands and spin-non-degenerate Dirac SSs, the bulk Rashba-type superconductivity may appear in the $m \geq 2$ samples. Next, we extrapolated the value of $H_{c2,\parallel}/H_P$ at $T = 0$ K from the $(H_{c2,\parallel}/H_P)$–(T/T_c) curves. In monolayer $NbSe_2$, the extracted $H_{c2,\parallel}(T = 0\ \text{K})$ value is greater than 4.9 times the Pauli limit H_P, confirming the Ising-type pairing in monolayer $NbSe_2$. By depositing mQL Bi_2Se_3 films on monolayer $NbSe_2$, $H_{c2,\parallel}(T = 0\ \text{K})/H_P$ is reduced to ~3.4 for $m = 1$ and ~2.0 for $2 \leq m \leq 6$. The value of $H_{c2}(T = 0\ \text{K})/H_P$ greater than the factor of $\sqrt{2}$ in the $2 \leq m \leq 6$ samples provides further evidence that bulk Rashba-type superconductivity takes over from the Ising-type behaviour in Bi_2Se_3/monolayer $NbSe_2$ heterostructures[32].

The temperature dependence of $H_{c2,\perp}$ provides additional insights into the superconductivity in Bi_2Se_3/monolayer $NbSe_2$

https://doi.org/10.1038/s41563-022-01386-z

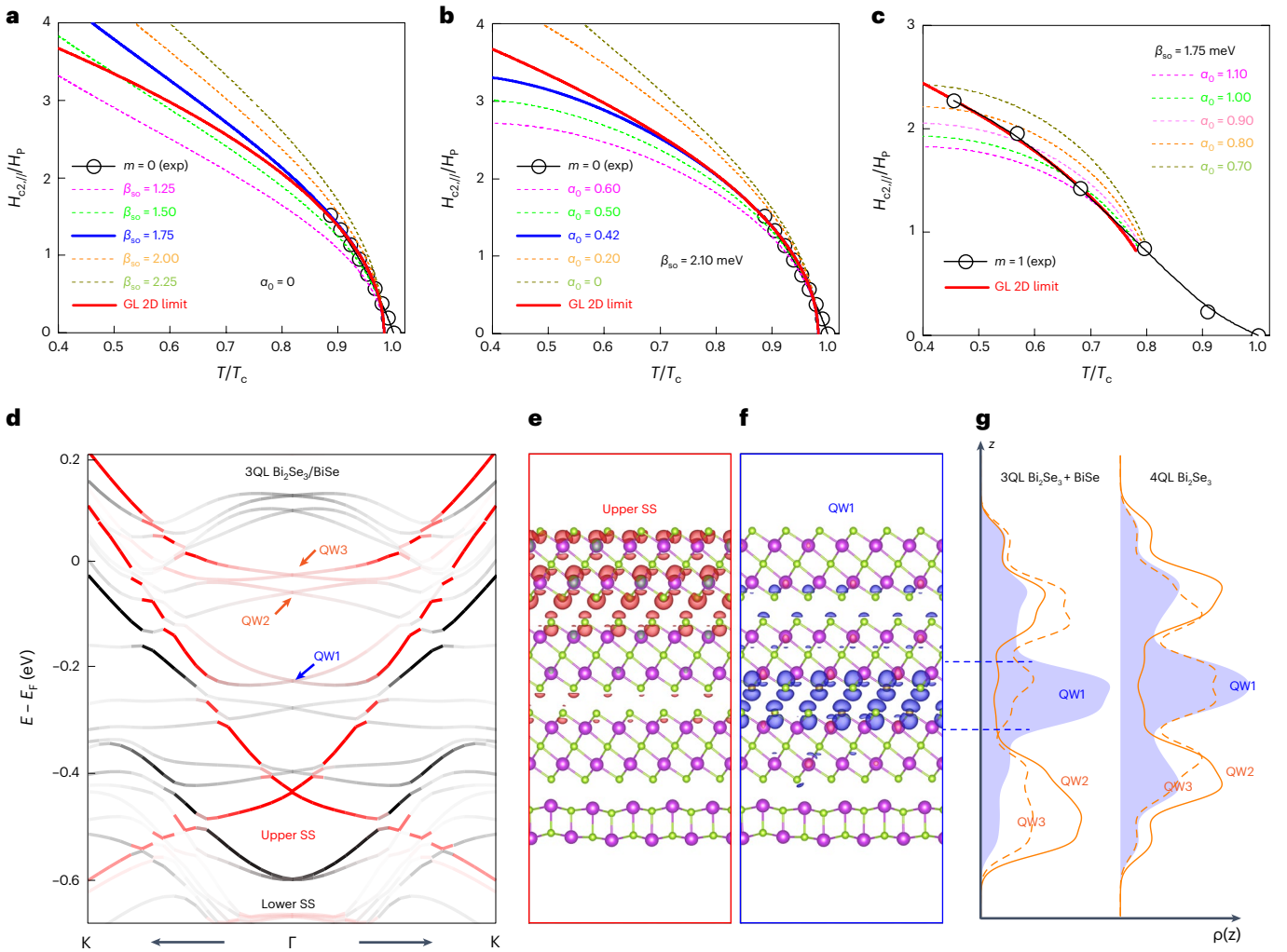

Fig. 4 | Theoretical calculations of Bi_2Se_3/monolayer $NbSe_2$ heterostructures. **a**–**c**, Calculated in-plane upper critical magnetic field normalized to the Pauli paramagnetic field $H_{c2,\parallel}/H_P$ as a function of normalized temperature T/T_c under different Ising-type spin–orbit coupling strengths β_{so} and Rashba-type spin–orbit coupling energies α_0. In **a**, for the $m = 0$ sample, we considered β_{so} from 1.25 to 2.25 meV and $\alpha_0 = 0$. The best fit is approached with $\beta_{so} = 1.75$ meV and $\Delta T_c = -0.04$ K (blue solid line) for our experimental data (black circles), consistent with the GL 2D limit fit near T_c (red solid line). In **b**, we included a small α_0 value from 0 to 0.6 meV with fixed $\beta_{so} = 2.1$ meV for the $m = 0$ sample. The best fit is achieved for a weak $\alpha_0 = 0.42$ meV, indicating that the Ising-type Cooper pairs are still dominant in the $m = 0$ sample. In **c**, the experimental data of the $m = 1$ sample cannot be fitted by either linear-T behaviour (GL 3D limit) or square-root-T behaviour (GL 2D limit; red solid line). A moderate fit with two comparable spin–orbit-coupling parameters, that is, $\alpha_0 \approx 0.9$ meV and $\beta_{so} \approx 1.75$ meV, indicates the occurrence of crossover from 2D Ising-type to 3D bulk Rashba-type superconductivity in the $m = 1$ sample. **d**, Calculated band structure of 3QL Bi_2Se_3/BiSe heterostructure. The projections of the total wavefunction onto Bi orbitals on the upper and lower surfaces of 3QL Bi_2Se_3 are shown in red and black. More Rashba-type QW states in bulk conduction bands are marked by arrows. **e**,**f**, Partial charge densities for the upper SS (**e**) and the first QW state (**f**). **g**, Charge densities averaged in the x–y plane plotted along z, for the three QW states in 3QL Bi_2Se_3/BiSe heterostructure and the three QW states in a freestanding 4QL Bi_2Se_3 film.

heterostructures. We found that the $(H_{c2,\perp}/H_P)$–(T/T_c) curves display a linear behaviour in both monolayer $NbSe_2$ and mQL Bi_2Se_3/monolayer $NbSe_2$ heterostructures due to the constraint of the orbital-pair-breaking effect (Fig. 3c). As noted above, the Rashba-type superconductivity emerges in the $2 \le m \le 6$ samples, where the spins of two electrons are pinned to the in-plane direction (Fig. 1d). However, with an out-of-plane magnetic field, the orbital effect dominates, allowing the breaking of Cooper pairing. As a consequence, the enhancement in $H_{c2,\perp}$ was not observed in these bulk Rashba-type superconductors (Fig. 3c). We used the Ginzburg–Landau (GL) expression $H_{c2,\perp} = \Phi/(2\pi\xi^2_{GL,\perp})$ to calculate the out-of-plane GL coherence length $\xi_{GL,\perp}$ from $H_{c2,\perp}(T = 0\ \mathrm{K})$. Here Φ is the magnetic flux quantum. The value determined for monolayer $NbSe_2$, namely, $\xi_{GL,\perp} \approx 14$ nm, is consistent with that found in bulk $NbSe_2$ crystals[4]. The value of $\xi_{GL,\perp}$ continuously increases with increasing m, suggesting that proximity-induced superconductivity occurs on both interior and top surface of Bi_2Se_3 films even in the $m = 6$ sample. A proximity-induced superconducting gap on both top and bottom Dirac SSs is a prerequisite for creating the TSC phase in TI/superconductor heterostructures[1]. For the $m = 6$ sample, $\xi_{GL,\perp}$ is found to be ~57 nm (Fig. 3c, inset). A similar enhancement in $\xi_{GL,\perp}$ has been observed in proximity-induced superconductivity in Bi_2Te_3/bulk $NbSe_2$ heterostructures[4]. As a result, we posited that the proximity-induced superconducting gap occurs in both Rashba-type bulk bands and spin-non-degenerate Dirac SSs of the Bi_2Se_3 layer. This leads to bulk Rashba-type superconductivity in the $m \ge 6$ samples. In addition to $\xi_{GL,\perp}$, the in-plane GL coherence length $\xi_{GL,\parallel}$ deduced from $H_{c2,\parallel}(T = 0\ \mathrm{K})$ also continuously increases with increasing m, further confirming the appearance of proximity-induced superconductivity on the top surface of TI films (Fig. 3b, inset).

To understand our transport results, we theoretically analysed $H_{c2,\parallel}$ by considering the Zeeman coupling of monolayer $NbSe_2$. The Ising-type superconductivity in monolayer $NbSe_2$ serves as the Cooper

pairing source for the bulk superconductivity in mQL Bi_2Se_3/$NbSe_2$ heterostructures. A strong Ising-type spin–orbit coupling ($\beta_{so} \approx 1.75$ meV) protects the superconducting states against the de-pairing term of the in-plane magnetic field, which gives rise to a large $H_{c2,\parallel}/H_P$. The enhanced paramagnetic limit[33] is described by

$$\log\left[\frac{T}{T_c}\right] = \mathrm{Re}\left[\psi^{(0)}\left(\frac{1}{2}\right) - \psi^{(0)}\left(\frac{1}{2} + \mathrm{i}\frac{\sqrt{\beta_{so}^2 + H_x^2}}{2\pi k_B T}\right)\right] \times \frac{H_x^2}{\beta_{so}^2 + H_x^2}, \quad (1)$$

where $\psi^{(0)}(z)$ is the digamma function, k_B is the Boltzmann constant and H_x is the Zeeman energy. We first used equation (1) to fit the $(H_{c2,\parallel}/H_P)$–(T/T_c) curves of the monolayer $NbSe_2$ film with a single Ising-type spin–orbit coupling parameter β_{so} and achieved the best fit with $\beta_{so} \approx 1.75$ meV (Fig. 4a). We next examined the influence of Rashba-type spin–orbit coupling on the upper critical field (equation (8)), and with two fitting parameters, namely, β_{so} and $\alpha_0 = \alpha_R k_F$. The Rashba parameter α_0 reduces the upper critical field; thus, with a finite α_0, one has to also increase β_{so} to achieve a good fit. Figure 4b shows a fit for $\beta_{so} \approx 2.1$ meV with different α_0 values, and the best fit is achieved with $\alpha_0 \approx 0.42$ meV, which is much smaller than β_{so}, that is, $\alpha_0 < \beta_{so}/5$. Therefore, our theoretical calculations demonstrate that the 2D superconductivity in monolayer $NbSe_2$ carries Ising-type dominant Cooper pairs. For the $m = 1$ sample, the temperature dependence of the upper critical magnetic field deviates from either linear-T (GL 3D limit) or square-root-T (GL 2D limit) behaviour, suggesting a complicated crossover behaviour from a 2D Ising-type superconductor to a 3D bulk Rashba-type superconductor in this sample (Fig. 4c). The comparison between the theoretical model calculations and experimental data for the $m = 1$ sample is shown in Fig. 4c. The experimental data fall into the regime with the Rashba parameter of $\alpha_0 \approx$ ~0.7–1.1 meV, which is comparable to $\beta_{so} \approx 1.75$ meV. The discrepancy between theory and experiment is attributed to the 3D orbital effects that are not captured in our 2D model. In the Supplementary Information, we discussed another mechanism of intervalley scattering that can also suppress $H_{c2,\parallel}$ due to the interfacial cubic BiSe bilayer (Supplementary Fig. 3).

To identify the origin of the strong Rashba effect and the concurrent reduction in the 2D to 3D TI crossover thickness in mQL Bi_2Se_3/BiSe/monolayer $NbSe_2$ heterostructures, we performed first-principles calculations to examine the bulk QW bands and Dirac SSs. Capturing the entire Bi_2Se_3/BiSe/$NbSe_2$ heterostructure in first-principles calculations is challenging because a supercell commensurate with two different hexagonal lattices and a third cubic one is required. We instead examined two pairs of BiSe/$NbSe_2$ and Bi_2Se_3/BiSe. The electronic structure of BiSe/monolayer $NbSe_2$ shows that the band-filling occupation of the monolayer $NbSe_2$ layer does not show any substantial change (~0.04e per $NbSe_2$ formula unit) (Extended Data Fig. 8), consistent with our ARPES observation (Extended Data Fig. 3). This negligible charge transfer across BiSe/$NbSe_2$ leaves the hole carriers in the $NbSe_2$ layer uncompensated, which can still support the presence of superconductivity. Therefore, our following calculation of Bi_2Se_3/BiSe is a valid structural approximation of the mQL Bi_2Se_3/BiSe/monolayer $NbSe_2$ heterostructures.

Figure 4d shows the orbital-projected band structure of the 3QL Bi_2Se_3/BiSe heterostructure. For $-0.6 \le (E - E_F) \le -0.4$ eV, two Dirac SSs appear at different energies. The upper SS remains mostly intact, localized at the upper surface, whereas the lower SS drops to a lower-energy level due to its interaction with the BiSe layer but has an increased decay length (Fig. 4e and Supplementary Fig. 4). Therefore, we can attribute the energy separation of the two Dirac SSs to the interaction between the lower Dirac SS and BiSe layer, which relieves the lower Dirac SS from further hybridizing with the upper Dirac SS. This explains why the critical thickness for the 2D to 3D TI crossover in Bi_2Se_3/monolayer $NbSe_2$ heterostructures is reduced. For $-0.25 \le (E - E_F) \le 0$ eV, three QW bands labelled QW1, QW2 and QW3 appear, consistent with their x–y-plane-averaged partial charge densities having 0, 1 and 2 nodes, respectively (Fig. 4g). QW1 and QW2 are located at ~0.22 and ~0.39 eV above the Dirac point of the upper SS, respectively, in good agreement with the corresponding values of ~0.23 and ~0.44 eV determined from the ARPES band map for the $m = 3$ sample (Fig. 2c,i). The calculated Rashba splitting E_R of QW1 is ~0.009 eV (Supplementary Fig. 5), which is also close to the value of $E_R \approx 0.011$ eV measured by ARPES. Since mQL Bi_2Se_3 films usually produce $(m - 1)$ QW states above the conduction band minimum (Extended Data Fig. 9), the three QW states suggest that the $m = 3$ sample is effectively equivalent to a freestanding 4QL Bi_2Se_3 sample (Extended Data Fig. 10). In other words, the BiSe layer electronically resembles an additional Bi_2Se_3 layer. This is further confirmed by comparing the three QW states in the 3QL Bi_2Se_3/BiSe heterostructure with those in the freestanding 4QL Bi_2Se_3 sample (Fig. 4g). However, the 3QL Bi_2Se_3/BiSe heterostructure is different from the freestanding 4QL Bi_2Se_3 because the crystal potential of the former structure is asymmetric along z, as reflected from their partial charge densities plotted along z (Fig. 4g). Therefore, the presence of the interfacial BiSe layer facilitates the formation of bulk Rashba-type QW bands with large α_R by introducing a compositional gradient along z (Supplementary Fig. 6).

In summary, we fabricated superconducting Bi_2Se_3/monolayer $NbSe_2$ heterostructures by MBE and found that an interfacial BiSe layer with a cubic lattice structure is formed at the interface between the Bi_2Se_3 and monolayer $NbSe_2$ layers. By performing in situ ARPES measurements, we observed the formation of gapless Dirac SSs in the 3QL Bi_2Se_3/monolayer $NbSe_2$ heterostructure. Moreover, several bulk Rashba-type QW bands appear in Bi_2Se_3/monolayer $NbSe_2$ heterostructures with Bi_2Se_3 thickness greater than 2QL. By performing magnetoresistance measurements, we found that both in-plane and out-of-plane upper critical magnetic fields of the superconducting Bi_2Se_3/monolayer $NbSe_2$ heterostructures are greatly reduced with an increase in the Bi_2Se_3 film thickness, indicating the occurrence of a crossover from Ising- to bulk Rashba-type pairings. The successful synthesis of both Ising-type superconductor and TI films by MBE as well as the observation of crossover from Ising-type to bulk Rashba-type superconductivity may advance the exploration of the robust TSC phase in TI/Ising-type superconductor heterostructures.

Online content

Any methods, additional references, Nature Research reporting summaries, source data, extended data, supplementary information, acknowledgements, peer review information; details of author contributions and competing interests; and statements of data and code availability are available at https://doi.org/10.1038/s41563-022-01386-z.

References

1. Fu, L. & Kane, C. L. Superconducting proximity effect and Majorana fermions at the surface of a topological insulator. *Phys. Rev. Lett.* **100**, 096407 (2008).
2. Wang, M. X. et al. The coexistence of superconductivity and topological order in the Bi_2Se_3 thin films. *Science* **336**, 52–55 (2012).
3. Xu, S. Y. et al. Momentum-space imaging of Cooper pairing in a half-Dirac-gas topological superconductor. *Nat. Phys.* **10**, 943–950 (2014).
4. Xu, J. P. et al. Artificial topological superconductor by the proximity effect. *Phys. Rev. Lett.* **112**, 217001 (2014).
5. Xu, J. P. et al. Experimental detection of a Majorana mode in the core of a magnetic vortex inside a topological insulator-superconductor Bi_2Te_3/$NbSe_2$ heterostructure. *Phys. Rev. Lett.* **114**, 017001 (2015).
6. Sun, H. H. et al. Majorana zero mode detected with spin selective Andreev reflection in the vortex of a topological superconductor. *Phys. Rev. Lett.* **116**, 257003 (2016).

7. Zhu, Z. et al. Discovery of segmented Fermi surface induced by Cooper pair momentum. *Science* **374**, 1381–1385 (2021).
8. Xi, X. X. et al. Ising pairing in superconducting $NbSe_2$ atomic layers. *Nat. Phys.* **12**, 139–143 (2016).
9. Xing, Y. et al. Ising superconductivity and quantum phase transition in macro-size monolayer $NbSe_2$. *Nano Lett.* **17**, 6802–6807 (2017).
10. Hsu, Y. T., Vaezi, A., Fischer, M. H. & Kim, E. A. Topological superconductivity in monolayer transition metal dichalcogenides. *Nat. Commun.* **8**, 14985 (2017).
11. Xu, G., Wang, J., Yan, B. H. & Qi, X. L. Topological superconductivity at the edge of transition-metal dichalcogenides. *Phys. Rev. B* **90**, 100505 (2014).
12. Zhou, B. T., Yuan, N. F. Q., Jiang, H. L. & Law, K. T. Ising superconductivity and Majorana fermions in transition-metal dichalcogenides. *Phys. Rev. B* **93**, 180501 (2016).
13. Chang, C. Z. et al. Growth of quantum well films of topological insulator Bi_2Se_3 on insulating substrate. *SPIN* **1**, 21–25 (2011).
14. Zhang, Y. et al. Crossover of the three-dimensional topological insulator Bi_2Se_3 to the two-dimensional limit. *Nat. Phys.* **6**, 584–588 (2010).
15. Sakamoto, Y., Hirahara, T., Miyazaki, H., Kimura, S. & Hasegawa, S. Spectroscopic evidence of a topological quantum phase transition in ultrathin Bi_2Se_3 films. *Phys. Rev. B* **81**, 165432 (2010).
16. Yokoya, T. et al. Fermi surface sheet-dependent superconductivity in 2H-$NbSe_2$. *Science* **294**, 2518–2520 (2001).
17. Zhang, H. J. et al. Topological insulators in Bi_2Se_3, Bi_2Te_3 and Sb_2Te_3 with a single Dirac cone on the surface. *Nat. Phys.* **5**, 438–442 (2009).
18. Xia, Y. et al. Observation of a large-gap topological-insulator class with a single Dirac cone on the surface. *Nat. Phys.* **5**, 398–402 (2009).
19. Wang, M. X. et al. Interface structure of a topological insulator/superconductor heterostructure. *New J. Phys.* **16**, 123043 (2014).
20. Ugeda, M. M. et al. Characterization of collective ground states in single-layer $NbSe_2$. *Nat. Phys.* **12**, 92–97 (2016).
21. Xu, C. Z. et al. Experimental and theoretical electronic structure and symmetry effects in ultrathin $NbSe_2$ films. *Phys. Rev. Mater.* **2**, 064002 (2018).
22. Liu, C. X. et al. Oscillatory crossover from two-dimensional to three-dimensional topological insulators. *Phys. Rev. B* **81**, 041307 (2010).
23. Sattar, S. & Larsson, J. A. Tunable electronic properties and large Rashba splittings found in few-layer $Bi_2Se_3/PtSe_2$ van der Waals heterostructures. *ACS Appl. Electron. Mater.* **2**, 3585–3592 (2020).
24. Zhu, Z. H. et al. Rashba spin-splitting control at the surface of the topological insulator Bi_2Se_3. *Phys. Rev. Lett.* **107**, 186405 (2011).
25. Valla, T., Pan, Z. H., Gardner, D., Lee, Y. S. & Chu, S. Photoemission spectroscopy of magnetic and nonmagnetic impurities on the surface of the Bi_2Se_3 topological insulator. *Phys. Rev. Lett.* **108**, 117601 (2012).
26. King, P. D. C. et al. Large tunable Rashba spin splitting of a two-dimensional electron gas in Bi_2Se_3. *Phys. Rev. Lett.* **107**, 096802 (2011).
27. Bahramy, M. S. et al. Emergent quantum confinement at topological insulator surfaces. *Nat. Commun.* **3**, 1159 (2012).
28. Buzdin, A. I. Proximity effects in superconductor-ferromagnet heterostructures. *Rev. Mod. Phys.* **77**, 935–976 (2005).
29. Wördenweber, R., Moshchalkov, V. V., Bending, S. J. & Tafuri, F. *Superconductors at the Nanoscale: From Basic Research to Applications* (de Gruyter, 2017).
30. Xi, X. X., Berger, H., Forro, L., Shan, J. & Mak, K. F. Gate tuning of electronic phase transitions in two-dimensional $NbSe_2$. *Phys. Rev. Lett.* **117**, 106801 (2016).
31. Ruggiero, S. T., Barbee, T. W. & Beasley, M. R. Superconductivity in quasi-two-dimensional layered composites. *Phys. Rev. Lett.* **45**, 1299–1302 (1980).
32. Yoshizawa, S. et al. Atomic-layer Rashba-type superconductor protected by dynamic spin-momentum locking. *Nat. Commun.* **12**, 1462 (2021).
33. Lu, J. M. et al. Evidence for two-dimensional Ising superconductivity in gated MoS_2. *Science* **350**, 1353–1357 (2015).

Methods

MBE growth

The Bi_2Se_3/monolayer $NbSe_2$ heterostructures used in this work were grown on bilayer-graphene-terminated 6H-SiC (0001) substrates in an MBE chamber (Scienta Omicron) with a vacuum better than 2×10^{-10} mbar. For the MBE growth of monolayer $NbSe_2$, the substrate temperature was kept at 500 °C. The monolayer $NbSe_2$ was post-annealed at 600 °C for 30 min to improve its crystallinity. Next, the Bi_2Se_3 films were grown on monolayer $NbSe_2$ at ~150 °C. This low growth temperature is crucial for achieving superconductivity in Bi_2Se_3/monolayer $NbSe_2$ heterostructures. The MBE growth process was monitored by reflection high-energy electron diffraction (Extended Data Fig. 1). The samples were capped with a 10 nm Se layer to prevent their degradation during the ex situ electrical transport measurements.

ADF-STEM measurements

The aberration-corrected ADF-STEM measurements were performed on an FEI Titan^3 G2 STEM operating at an accelerating voltage of 300 kV, with a probe convergence angle of 25 mrad, probe current of 100 pA and ADF detector angles of ~42–244 mrad. Extended Data Fig. 2 shows more STEM images of Bi_2Se_3/monolayer $NbSe_2$ heterostructures.

ARPES measurements

The in situ ARPES measurements were performed at room temperature after transferring the samples from the MBE chamber. A hemispherical Scienta DA30L analyser was used, and the photoelectrons were excited by a helium discharged lamp with a photon energy of ~21.2 eV. The energy and angle resolution were set at ~10 meV and ~0.1°, respectively.

Electrical transport measurements

The electrical transport measurements were carried out in a physical property measurement system (Quantum Design DynaCool; 2 K and 9 T), a Heliox ^{3}He refrigerator (Oxford Instruments; 400 mK and 6 T) and a dilution refrigerator (Bluefors; 20 mK and 9/1/1 T). Six-terminal mechanically defined Hall bars were used for the electrical transport studies.

First-principles calculations

The first-principles calculations were performed using the Perdew–Burke–Ernzerhof parametrization of the generalized gradient approximation exchange–correlation functional[34]. Interactions between the electrons and nuclei were described by the projector augmented-wave pseudopotentials[35], as implemented in the Vienna ab initio simulation package[36]. Interlayer van der Waals interactions were accounted for using Grimme's DFT-D3 correction scheme[37]. Non-collinear spin textures and spin–orbit coupling were enabled following the native Vienna ab initio simulation package implementation. Convergence parameters included the following: a plane-wave expansion energy cutoff of 500 eV, a residual force threshold of 0.01 eV Å^{-1} for relaxations (except for *m*QL Bi_2Se_3 plus BiSe, as shown below), a $12 \times 12 \times 1$ *k*-point grid for multilayer Bi_2Se_3 unit-cell calculations and a $6 \times 1 \times 1$ *k*-point grid for Bi_2Se_3 plus BiSe calculations.

For Bi_2Se_3 plus BiSe calculations, a $1 \times 3\sqrt{3}$ trilayer Bi_2Se_3 plus 1×5 cubic BiSe supercell was chosen, where Bi_2Se_3 adopted its native lattice constant of 4.14 Å, requiring cubic BiSe to accommodate by sustaining a slight strain (1.6% and 2.2% in the lateral directions, considering BiSe's native lattice constant of 4.21 Å). This favouritism towards Bi_2Se_3 was to ensure the accuracy of the low-energy electronic structure of the heterostructure, dominated by Bi_2Se_3 bands (to be compared with experiments), and is also justified by the larger thickness of Bi_2Se_3 than BiSe. Structural relaxations for Bi_2Se_3 plus BiSe were prematurely terminated where residual forces were still ~0.2 eV Å^{-1}; at this stage, the softest degrees of freedom (Bi_2Se_3–BiSe interlayer separation) had already stabilized and resumed relaxation would strongly distort the BiSe layer through the formation of strong bonds between Bi (in BiSe) and Se (in Bi_2Se_3) wherever a Bi(BiSe)/Se(Bi_2Se_3) pair happened to be close in the supercell. In a realistic structure including the underlying $NbSe_2$ and graphene substrate, such distortions would be suppressed since they would inflict additional energy penalty in interlayer adhesion and bending at the BiSe/$NbSe_2$ interface. Although a full relaxation with a near-commensurate supercell containing all the structural components (that is, Bi_2Se_3, BiSe, $NbSe_2$ and graphene) would be ideal, it would also require >1,000 atoms (with spin–orbit coupling) and is therefore beyond our computational capabilities. For this reason, we used a flat Bi_2Se_3 plus BiSe structure in all the electronic structure calculations.

Theoretical calculations of critical temperature and upper critical magnetic fields

To achieve the best fit for our experimental data of the monolayer $NbSe_2$ sample, we took an adjustment of T_c with a 3% error from the experimental data into account. It means T_c achieved in our experiments might be replaced by

$$T_c' = T_c + \Delta T_c. \tag{2}$$

From the GL theory in the 2D limit, we know that

$$b_0 \left(\frac{H}{H_P}\right)^2 = 1 - \frac{T(H)}{T_c'} = 1 - \frac{T(H)}{T_c + \Delta T_c}. \tag{3}$$

This leads to

$$\frac{T(H)}{T_c + \Delta T_c} = 1 - b_0 \left(\frac{H}{H_P}\right)^2, \tag{4}$$

which can be rewritten as

$$\frac{T(H)}{T_c} = \frac{T_c + \Delta T_c}{T_c}\left[1 - b_0 \left(\frac{H}{H_P}\right)^2\right] \tag{5}$$

for the fitting process. Here there are two fitting parameters, namely, b_0 and ΔT_c. During the fitting process, $|\Delta T_c|$ is less than $3\% T_c$.

In addition to the GL theory, we also adopted a model calculation to fit the in-plane upper critical field $H_{c2,\parallel}$ to reveal the role of the Ising-type spin–orbit coupling β_{so} in our experiments. We considered the normal Hamiltonian of monolayer $NbSe_2$ around the K and K′ valleys[33] as

$$H_0 = \left(\frac{p^2}{2m_h} - \mu\right)\tau_0 s_0 + \beta_{so}\tau_z s_z + \alpha_R (p_x s_y - p_y s_x) + H_x s_x, \tag{6}$$

where m_h is the effective mass, and τ and s are Pauli matrices in the valley and spin subspace, respectively. A phenomenological interaction Hamiltonian is considered to induce a spin-singlet intervalley pairing state[33]. Note that the spin-triplet components induced by spin–orbit coupling are in the order of $\beta_{so}/\mu \ll 1$, which can be ignored for simplicity[33].

To study the relationship between the in-plane upper critical magnetic field $H_{c2,\parallel}$ and critical temperature T/T_c, we used the standard GL theory and solved the linearized gap equation[38]

$$\frac{1}{\upsilon_0} = -k_B T \sum_{i\omega_n, p} \left[(\tau_x s_y) G_e (i\omega_n, p)(\tau_x s_y) G_h(i\omega_n, -p)\right], \tag{7}$$

where υ_0 is the dimensionless attractive interaction strength, $G_e(i\omega_n, p) = [i\omega_n - H_0(p)]^{-1}$ is the Matsubara Green's function for electrons and $G_h = -G_e^*$ for holes.

We first considered a simple limit with $\alpha_R = 0$; then, the solution of equation (7) gives rise to equation (1), which explains why the Ising-type superconductivity is resilient to an in-plane pair-breaking magnetic

field. For monolayer $NbSe_2$, the best fit is achieved with $\beta_{so} = 1.75$ meV. Under a weak magnetic field, the factor $H_x^2/(\beta_{so}^2 + H_x^2) \ll 1$induces a large in-plane $H_{c2,\parallel} \gg H_P$.

Next, we included the Rashba-type spin–orbit coupling α_0 that competes with β_{so} (ref. [33]); then, the solution of equation (7) becomes

$$\log\left[\frac{T}{T_c}\right] = \frac{1}{2}\left[C_0(\rho_-) + C_0(\rho_+)\right] + \frac{1}{2}\left[C_0(\rho_-) - C_0(\rho_+)\right] \times \frac{\beta_{so}^2 + \alpha_0^2 - H_x^2}{E_- E_+}, \quad (8)$$

where $E_\pm = \sqrt{\beta_{so}^2 + (H_x \pm \alpha_0)^2}$, $\alpha_0 = \alpha_R k_F$ and k_F is the Fermi momentum, that is, $\rho_\pm = \frac{1}{2}(E_+ \pm E_-)$ The kernel of the de-pairing function in equation (8) is given by $C_0(x) = \mathrm{Re}\left[\psi^{(0)}\left(\frac{1}{2}\right) - \psi^{(0)}\left(\frac{1}{2} + i\frac{x}{2\pi k_B T}\right)\right]$, where $\psi^{(0)}(z)$ is the digamma function. Note that equation (8) can be reduced to equation (1) by setting $\alpha_0 = 0$. The presence of α_R increases the de-pairing term $\rho_\pm$, which, in turn, decreases the in-plane $H_{c2,\parallel}$. However, by fitting the experimental data of the monolayer $NbSe_2$ sample, we found that the Rashba-type spin–orbit coupling energy α_0 is much smaller than the Ising-type spin–orbit coupling β_{so}, that is, $\alpha_0 < \beta_{so}/5$, and thus, the Rashba effect can be ignored in monolayer $NbSe_2$ (Fig. 4b). Finally, we used equation (8) to investigate the paramagnetic pair-breaking effect for the $m = 1$ sample. The moderate fit shows $\beta_{so} = 1.75$ meV and $\alpha_0 = 0.90$ meV (Fig. 4c); these two comparable spin–orbit couplings indicate the occurrence of crossover from Ising-type (that is, the $m = 0$ sample) to Rashba-type (that is, the $m \geq 2$ sample) Copper pairs in Bi_2Se_3/monolayer $NbSe_2$ heterostructures.

Data availability

The datasets generated during and/or analysed during this study are available from the corresponding author upon reasonable request.

Code availability

The codes used in the theoretical simulations and calculations are available from the corresponding author upon reasonable request.

References

34. Perdew, J. P., Burke, K. & Ernzerhof, M. Generalized gradient approximation made simple. *Phys. Rev. Lett.* **77**, 3865–3868 (1996).
35. Blöhl, P. E. Projector augmented-wave method. *Phys. Rev. B* **50**, 17953–17979 (1994).
36. Kresse, G. & Furthmuller, J. Efficient iterative schemes for ab initio total-energy calculations using a plane-wave basis set. *Phys. Rev. B* **54**, 11169–11186 (1996).
37. Grimme, S., Antony, J., Ehrlich, S. & Krieg, H. A consistent and accurate ab initio parametrization of density functional dispersion correction (DFT-D) for the 94 elements H-Pu. *J. Chem. Phys.* **132**, 154104 (2010).
38. Sigrist, M. & Ueda, K. Phenomenological theory of unconventional superconductivity. *Rev. Mod. Phys.* **63**, 239–311 (1991).

Acknowledgements

We thank Y. Cui, K. T. Law and D. Xiao for helpful discussions. This work is primarily supported by the Penn State MRSEC for Nanoscale Science (DMR-2011839) (H.Y. and C.-Z.C.). The electrical transport measurements and sample characterization are partially supported by the NSF CAREER award (DMR-1847811) (C.-Z.C.). The theoretical calculations and simulations are partially supported by a DOE grant (DE-SC0019064) (C.-X.L.). Y.W. acknowledges support from a startup grant from the University of North Texas. The MBE growth and ARPES measurements were performed in the NSF-supported 2DCC MIP facility (DMR-2039351) (N.S. and C.-Z.C.). The dilution refrigerator transport measurements at University of Washington are supported by the AFOSR award (FA9550-21-1-0177) (X.X.) and acknowledge the usage of the millikelvin optoelectronic quantum material laboratory supported by the M. J. Murdock Charitable Trust. D.R.H. and N.A. acknowledge support from the NSF CAREER award (DMR-1654107). C.-Z.C. also acknowledges support from the Gordon and Betty Moore Foundation's EPiQS Initiative (grant GBMF9063 to C.-Z.C.).

Author contributions

C.-Z.C. conceived and designed the experiment. H.Y. performed the MBE growth and ARPES measurements and used the physical property measurement system with the help of Y.-F.Z., L.-J.Z., R.Z., A.R.R., M.H.W.C., N.S. and C.-Z.C. R.X. and H.Y. performed the ^{3}He transport measurements with the help of N.S. and C.-Z.C. J.C. and X.X. performed the dilution transport measurements. Y.W. performed the first-principles calculations. C.D. and J.A.R. prepared the bilayer graphene-terminated 6H-SiC(0001) substrates. D.R.H. and N.A. carried out the TEM measurements. L.-H.H. and C.-X.L. performed the theoretical simulations. H.Y., L.-H.H., Y.W. and C.-Z.C. analysed the data and wrote the manuscript with inputs from all the authors.

Competing interests

The authors declare no competing interests.

Additional information

Extended data is available for this paper at https://doi.org/10.1038/s41563-022-01386-z.

Supplementary information The online version contains supplementary material available at https://doi.org/10.1038/s41563-022-01386-z.

Correspondence and requests for materials should be addressed to Cui-Zu Chang.

Peer review information *Nature Materials* thanks Jinfeng Jia and the other, anonymous, reviewer(s) for their contribution to the peer review of this work.

https://doi.org/10.1038/s41563-022-01386-z

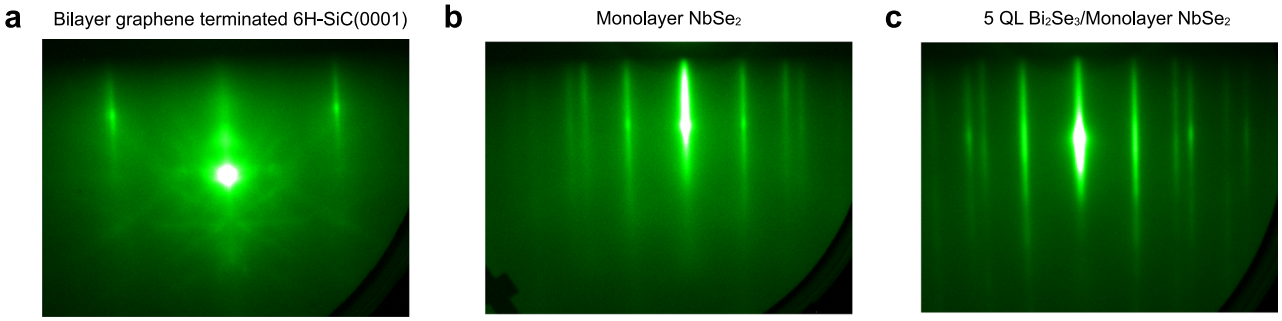

Extended Data Fig. 1 | RHEED patterns during MBE growth. (a) Bilayer graphene terminated 6H-SiC(0001) substrate. **(b)** Monolayer $NbSe_2$ film grown on bilayer graphene. **(c)** 5 QL Bi_2Se_3/monolayer $NbSe_2$ heterostructure grown on bilayer graphene.

https://doi.org/10.1038/s41563-022-01386-z

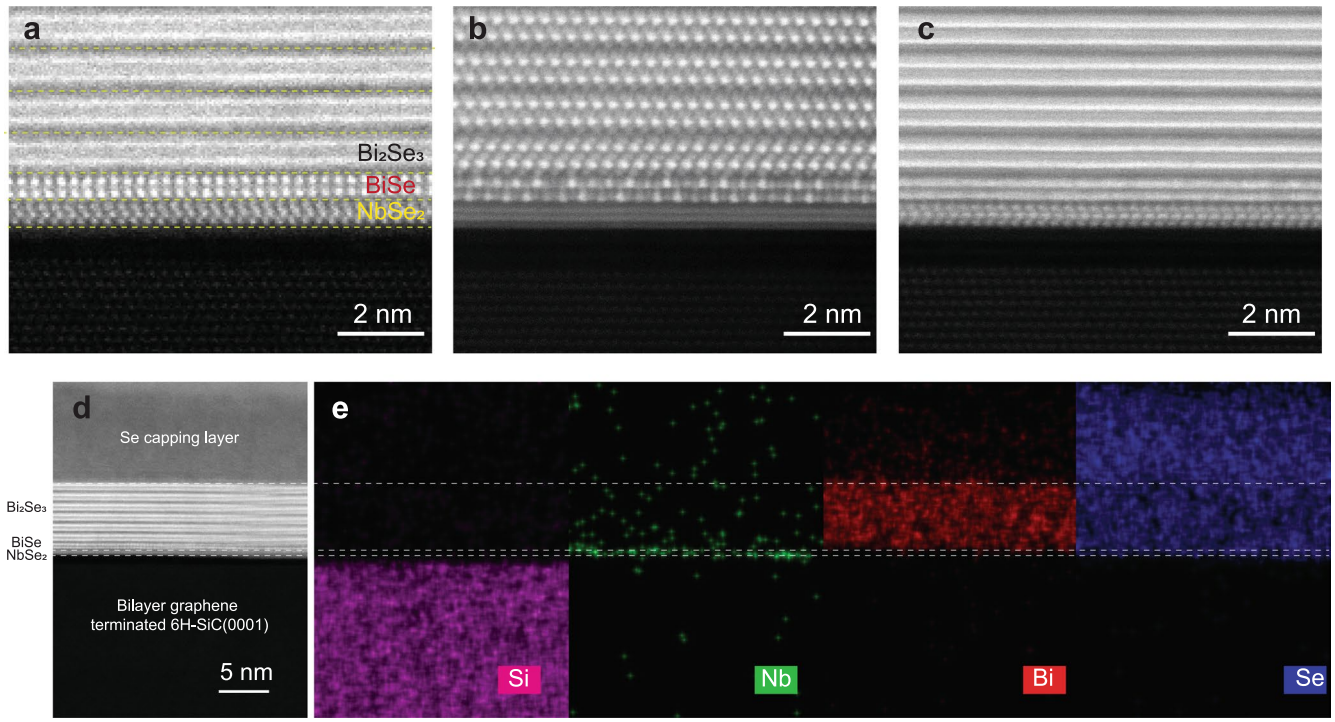

Extended Data Fig. 2 | Cross-sectional ADF-STEM images and EDS maps of the MBE-grown Bi_2Se_3/monolayer $NbSe_2$ heterostructure. (**a**–**c**) ADF-STEM images of the Bi_2Se_3/monolayer $NbSe_2$ heterostructure along different orientations. (d,e) Large-scale ADF-STEM image and corresponding EDS maps of Si, Nb, Bi, and Se of the Se layer-capped 6QL Bi_2Se_3/monolayer $NbSe_2$ heterostructure grown on bilayer graphene terminated 6H-SiC(0001).

https://doi.org/10.1038/s41563-022-01386-z

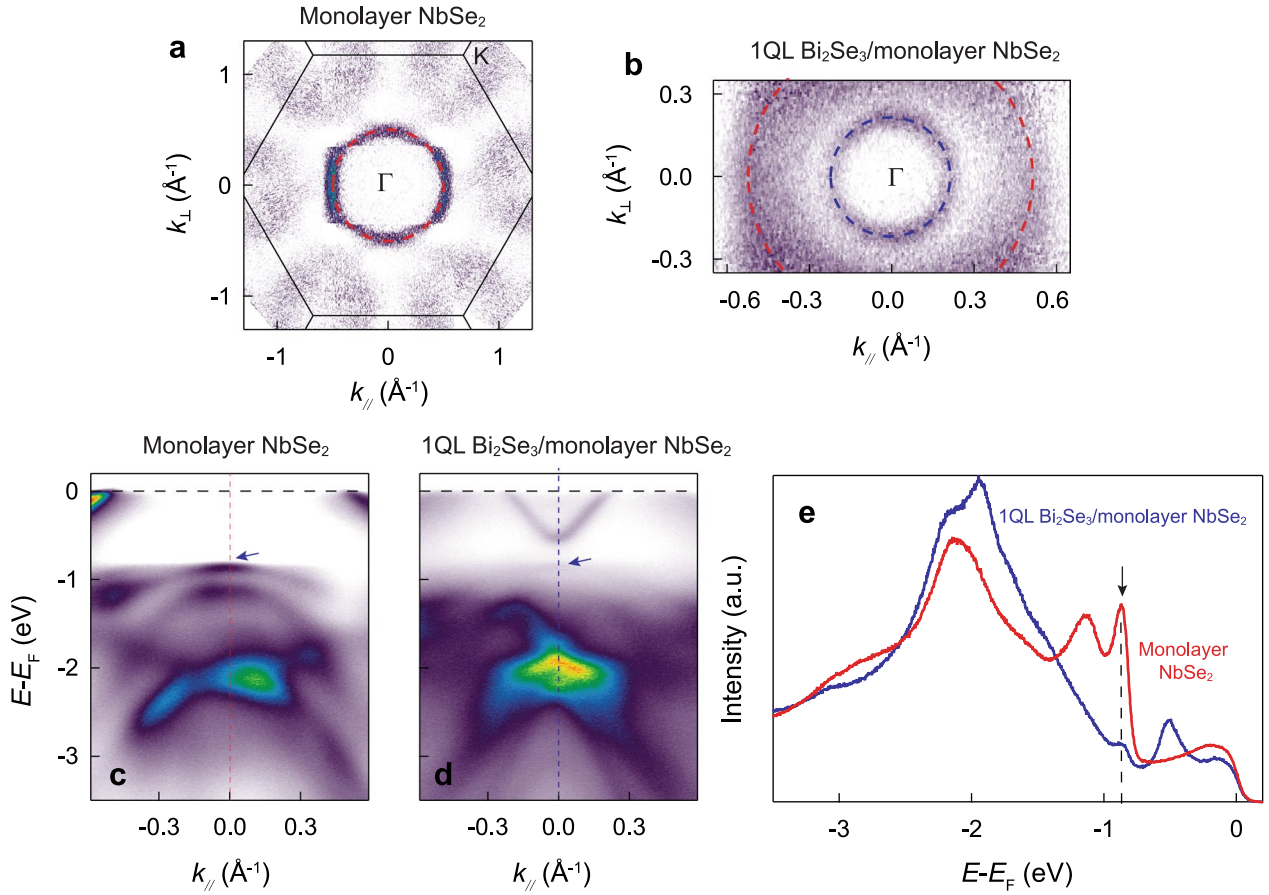

Extended Data Fig. 3 | Electronic band structures of monolayer $NbSe_2$ and 1QL Bi_2Se_3/monolayer $NbSe_2$. **(a)** Fermi surface of monolayer $NbSe_2$. **(b)** Fermi surface of 1QL Bi_2Se_3/monolayer $NbSe_2$. The red dashed lines in **(a)** and **(b)** locate the hole pocket near the Γ point from monolayer $NbSe_2$. The blue dashed line in **(b)** locates the electron pocket near the Γ point from 1QL Bi_2Se_3. (c, d) ARPES band maps of monolayer $NbSe_2$ and 1QL Bi_2Se_3/monolayer $NbSe_2$. **(e)** Comparison of the energy distribution curves at the Γ point in monolayer $NbSe_2$ (red line) and 1QL Bi_2Se_3/monolayer $NbSe_2$(blue line).

https://doi.org/10.1038/s41563-022-01386-z

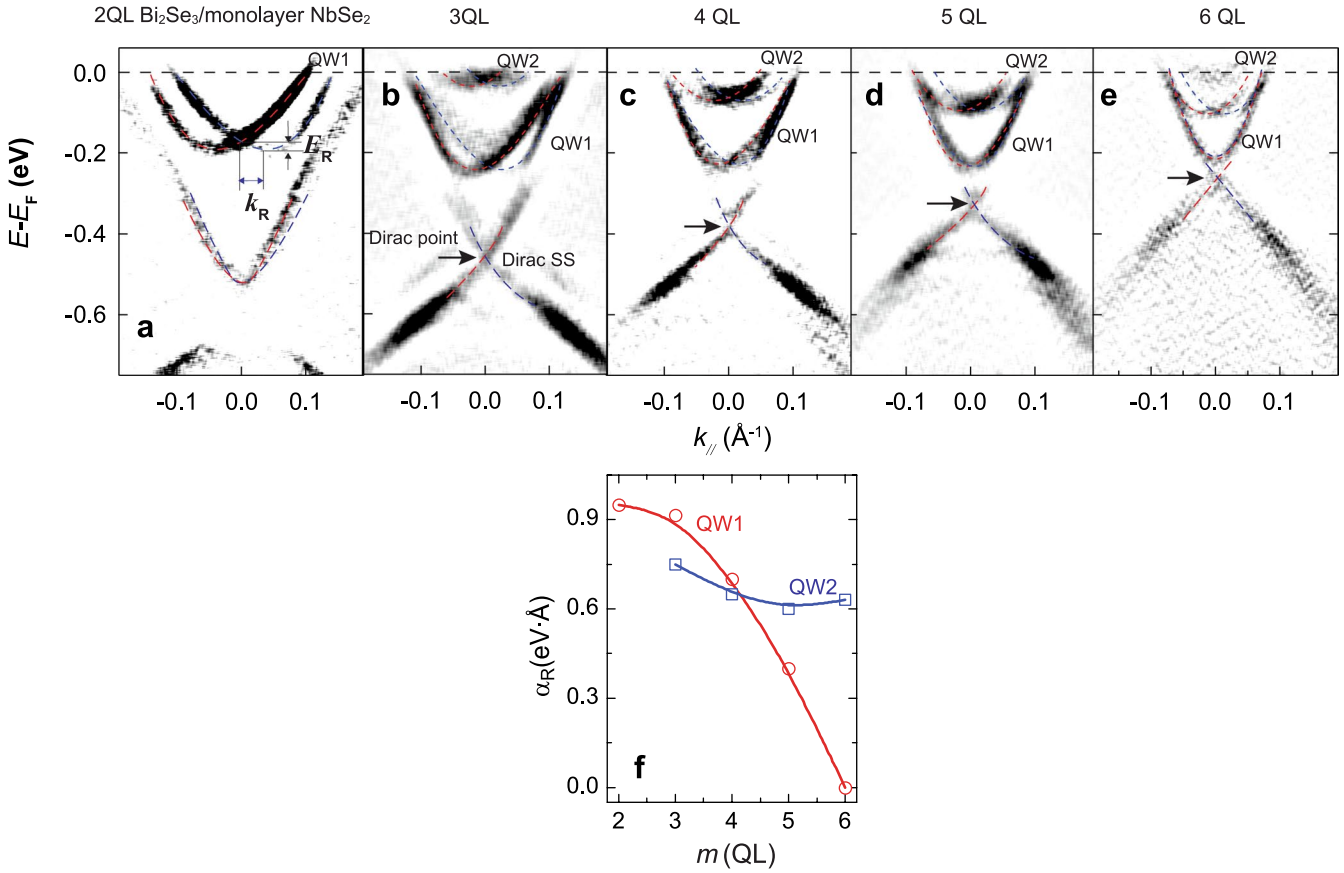

Extended Data Fig. 4 | Rashba-type bulk QW bands and Dirac SSs in *m*QL Bi_2Se_3/monolayer $NbSe_2$ heterostructures. (a-e) The second derivative spectra of the ARPES data in Fig. 2b–f of the main text. **(f)** Rashba splitting parameter α_R of QW1 and QW2 states as a function of *m*.

https://doi.org/10.1038/s41563-022-01386-z

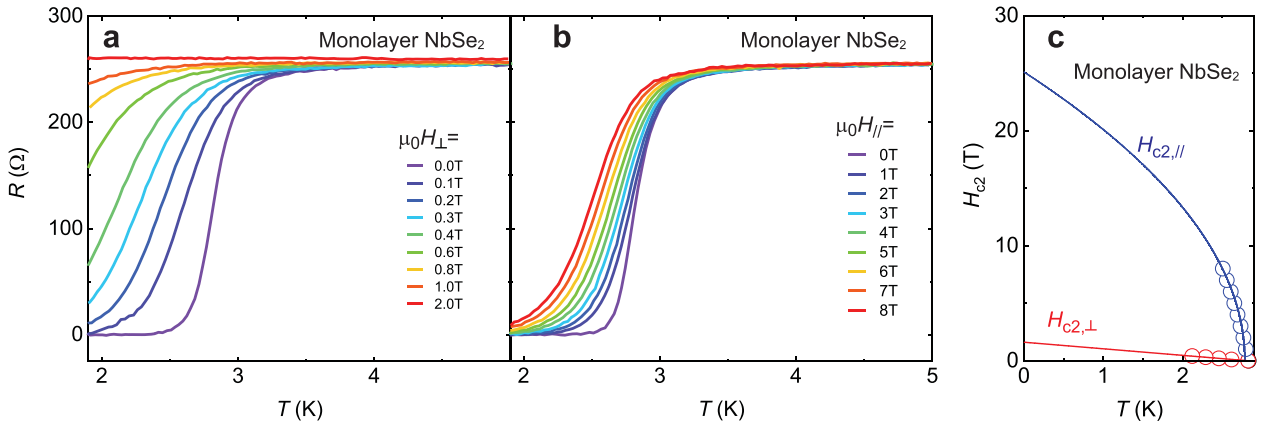

Extended Data Fig. 5 | Ising-type superconductivity in monolayer $NbSe_2$. **(a)** *R-T* curves of monolayer $NbSe_2$ under different out-of-plane magnetic fields $\mu_0 H_\perp$. **(b)** *R-T* curves of monolayer $NbSe_2$ under different in-plane magnetic fields $\mu_0 H_{||}$. **(c)** H_{c2}-*T* phase diagram of monolayer $NbSe_2$.

https://doi.org/10.1038/s41563-022-01386-z

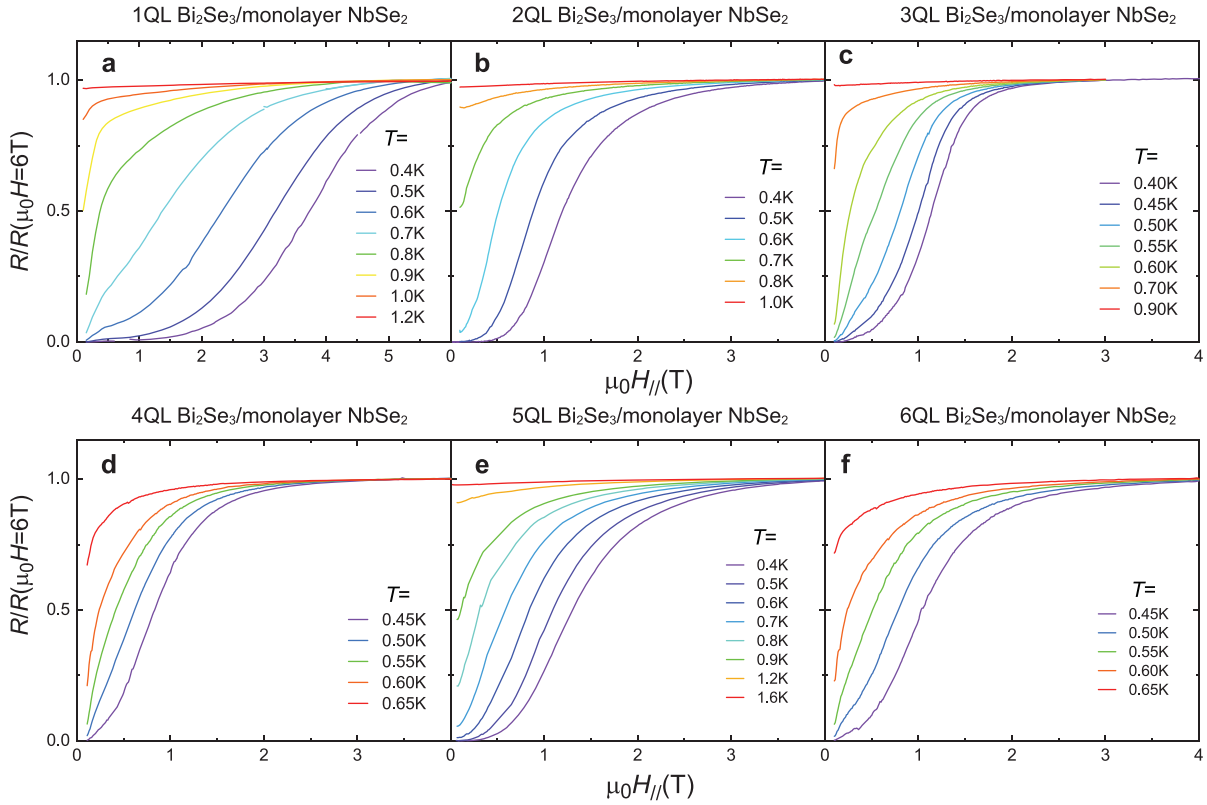

Extended Data Fig. 6 | *R*-$\mu_0 H$ curves of *m*QL Bi_2Se_3/monolayer $NbSe_2$ heterostructures under in-plane magnetic fields at different temperatures. **(a)** *m*=1. **(b)** *m*=2. **(c)** *m*=3. **(d)** *m*=4. **(e)** *m*=5. **(f)** *m*=6.

https://doi.org/10.1038/s41563-022-01386-z

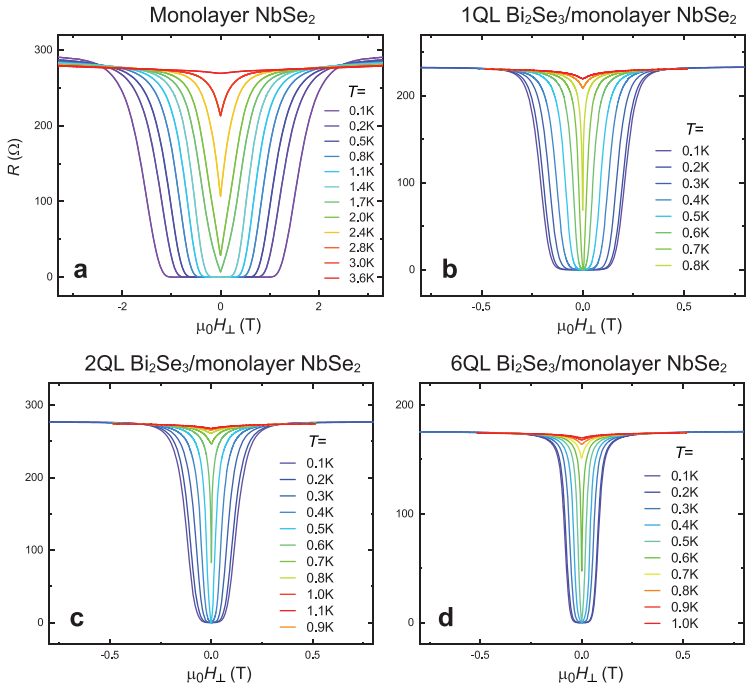

Extended Data Fig. 7 | R-$\mu_0 H$ curves of monolayer $NbSe_2$ and mQL Bi_2Se_3/$NbSe_2$ heterostructures under out-of-plane magnetic fields at different temperatures. **(a)** Monolayer $NbSe_2$. **(b)** m=1. **(c)** m=2. **(d)** m=6.

https://doi.org/10.1038/s41563-022-01386-z

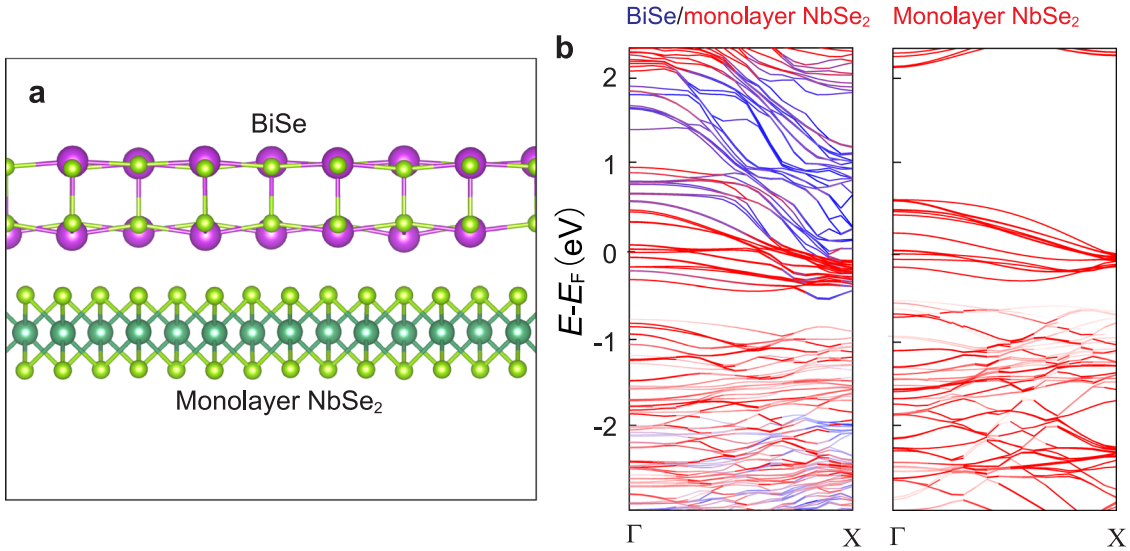

Extended Data Fig. 8 | Estimation of the charge transfer between monolayer $NbSe_2$ and BiSe. (a) Side view of calculation supercell for $\sqrt{2} \times 4\sqrt{2}$ BiSe on $\sqrt{3} \times 7$ $NbSe_2$. **(b)** Projected band structures of BiSe/monolayer $NbSe_2$ (left) and freestanding monolayer $NbSe_2$ (right). The projections of total wavefunction onto Nb orbitals and Bi orbitals are shown in red and blue, respectively.

https://doi.org/10.1038/s41563-022-01386-z

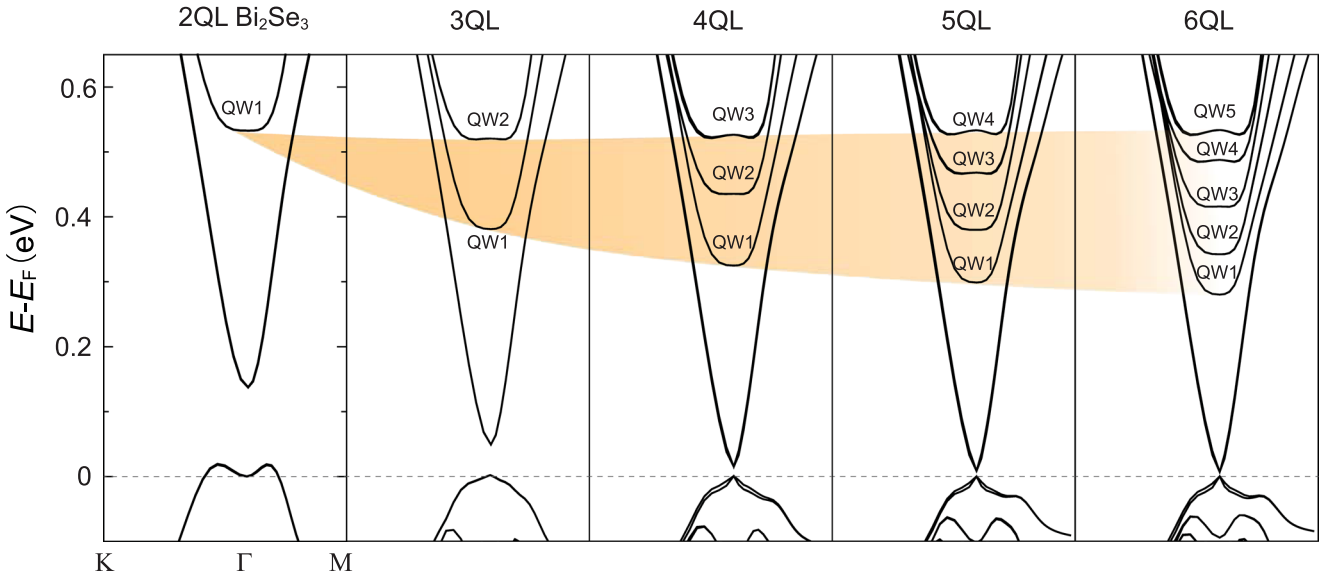

Extended Data Fig. 9 | (*m*−1) bulk QW states in *m*QL Bi_2Se_3 films. The calculated electronic band structures of freestanding *m*QL Bi_2Se_3 films with $2 \le m \le 6$.

https://doi.org/10.1038/s41563-022-01386-z

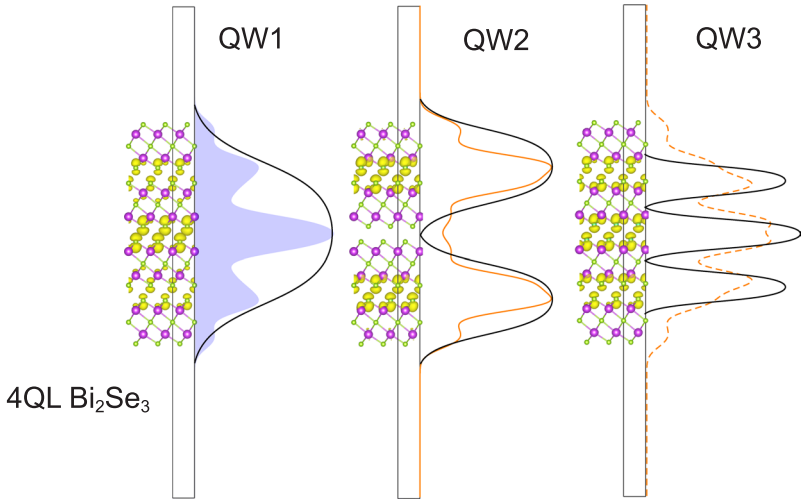

Extended Data Fig. 10 | Bulk QW states in a freestanding 4QL Bi_2Se_3 film. Partial charge densities for QW1, QW2, and QW3 in freestanding 4QL Bi_2Se_3 films, accompanied with their *xy*-plane-averaged representations $\rho_{xy}(z)$ plotted in the same way as Fig. 4g in the main text. Black curves are schematics for the charge densities of the envelope wavefunctions.